THE JOURNAL OF PHYSICAL CHEMISTRY LETTERS
A JOURNAL OF THE AMERICAN CHEMICAL SOCIETY

pubs.acs.org/JPCL Letter

Electronic State Mixing and Its Stimulated Raman Signature: A Case Study Using Free FMN and LOV Domain Proteins

Published as part of The Journal of Physical Chemistry Letters special issue "Future Leaders in Physical Chemistry".

Yingliang Liu,* Alessandra Picchiotti, Aditya S. Chaudhari, Mateusz Rebarz, Miroslav Kloz, Martin Precek, Jakob Andreasson, and Gustavo Fuertes

Cite This: https://doi.org/10.1021/acs.jpclett.5c04115 Read Online

ACCESS | Metrics & More | Article Recommendations | Supporting Information

ABSTRACT: In our previous investigation of the excited-state Raman spectra of free flavin mononucleotide (FMN) and the light-oxygen-voltage (LOV) sensitive protein EL222, we observed intensity variations and a red shift in the N_1-C_2 stretching modes within the S_1 state Raman spectroscopy of EL222. This phenomenon was attributed to potential S_1/S_2 state mixing. However, the existence of T_1/T_2 mixing in EL222 remained undetermined. To address this, we employed an avoided crossing model to simulate the influence of electronic state mixing on Raman spectroscopy. Our results indicate that mixing induces redshift or blueshift in the 0−1 Raman transition frequency and alters the equilibrium position, consequently affecting the corresponding Raman intensity. The analysis further suggests that S_1/S_2 state mixing in EL222 occurs within the weak coupling regime. Additionally, experimental data revealed potential Raman signatures indicative of T_1/T_2 mixing in EL222.

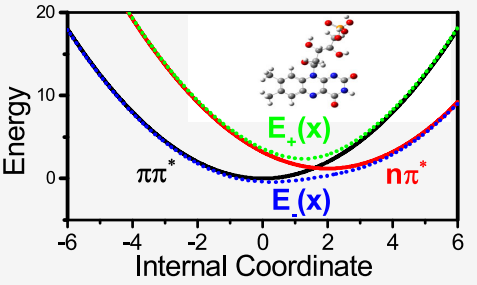

Electronic state mixing modifies the electron density distribution within molecules, leading to changes in permanent dipole moments and alterations to the potential energy surface, including molecular equilibrium geometry and force constants.[1−5] In specific cases, coupling between two electronic states can transform a conical intersection (CI) into an avoided crossing.

Recent advancements in ultrafast terahertz (THz) Stark spectroscopy have enabled tracking of electric interactions in solution.[6,7] In 2024, Zhang et al. applied this technique to bacteriorhodopsin and verified the occurrence of S_1/S_2 state mixing.[8] Evidence suggests that the substantial spectral tuning rates observed in green fluorescent protein (GFP) and photoactive yellow protein (PYP) chromophores also originate from electronic state mixing with charge-transfer states.[9−11]

Beyond alterations in dipole moments and spectral tuning rates, electronic state mixing influences chemical reaction dynamics. Haacke et al. compiled evidence demonstrating the impact of excited-state mixing on photoinduced C=C bond isomerization.[12] In the retinal protonated Schiff base (rPSB), strong mixing between the $1B_u$ charge-transfer state (S_1) and the $2A_g$ diradical state (S_2) introduces a slight barrier in the photoisomerization pathway and prolongs the S_1 state lifetime.[13,14] This $1B_u/2A_g$ mixing arises from steric distortions and electrostatic interactions within the protein binding pocket.

Time domain Raman spectroscopy techniques, including femtosecond stimulated Raman spectroscopy (FSRS)[15−17] and impulsive stimulated Raman spectroscopy (ISRS),[15−20] serve as powerful tools for monitoring structural changes in chromophores following photoexcitation.

Theoretical frameworks for spontaneous Raman intensity have been developed to elucidate molecular structures.[21−23] A methodology linking spontaneous resonance Raman band intensity to structural variations between electronic states has been established.[23−27] For stimulated Raman spectroscopy, a comparable relation between geometry differences and Raman band intensity using third-order nonlinear optical responses were derived.[28−30] This relation enables the extraction of relative Franck−Condon displacement amplitudes from fundamental Raman transition intensities. Recent advances now permit determination of absolute Franck−Condon displacements from resonance Raman signals via two-color broadband impulsive Raman experimental schemes.[31]

Light-oxygen-voltage (LOV) domain proteins function as environmental sensors across diverse biological kingdoms.[32−35] Multiple time-resolved experiments, including FSRS studies,[30,36−40] have been conducted on flavin[41,42] and flavin-

Received: December 31, 2025
Revised: February 24, 2026
Accepted: February 27, 2026

binding LOV domain proteins[43−51] to elucidate mechanisms underlying environmental response. Concurrently, numerous quantum chemistry simulations have explored the ground- and excited-state structures and dynamics of the flavin cofactor[52−58] both within and outside LOV domain proteins.[59−67]

In our prior work,[30] analysis of femtosecond stimulated Raman spectroscopy (FSRS) intensity variations in N_1-C_2 stretching modes following EL222 binding led us to propose potential electronic state mixing between the $\pi\pi^*(S_1)$ state and $n\pi^*(S_2)$ state of FMN within this LOV domain protein. Combining these findings with EL222 crystal structure data,[68,69] we hypothesize that symmetry breaking in hydrogen bonding interactions within the binding pocket facilitates nonzero coupling between these electronic states. Nevertheless, whether analogous state mixing occurs in the triplet state of FMN within EL222 remains an open question.

This study aims to address three fundamental questions: (1) How do changes in 0−1 Raman transition frequencies of local modes translate to delocalized normal modes? Specifically, can we deduce local mode 0−1 frequency shifts from normal mode shifts? (2) How does the change in the equilibrium position in the local mode propagate to normal modes and manifest in the Raman intensity? (3) Does electronic state mixing occur in the triplet state of EL222 similar to that observed in the singlet state?

Figure 1 illustrates an exemplary set of potential curves before electronic state mixing ($V_A(x)$ and $V_B(x)$ shown as black and red

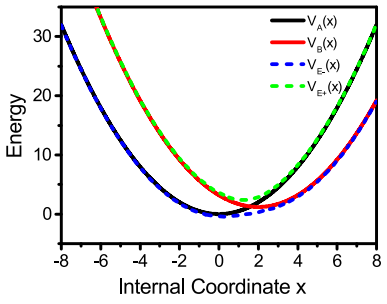

Figure 1. One set of example potential curves before and after electronic state mixing

solid lines) and after mixing $(V_{E_+})(x)$ and $V_{E_-}(x)$ depicted as green and blue dashed lines). In this example, the parameters are set to $x_{e,A} = 0$, $V_{e,A} = 0$; and $x_{e,B} = 2$, $V_{e,B} = 1.2$ with coupling constant $\beta = 1.2$.

In Figure 1, it is evident that the potential curve $V_{E_-}(x)$ is broader than the outer branches of the original $V_A(x)$ and $V_B(x)$ curves. This results in a red-shift of the 0−1 transition frequency associated with the potential $V_{E_-}(x)$. Conversely, $V_{E_+}(x)$ is located between the inner branches of the $V_A(x)$ and $V_B(x)$ curves. The potential $V_{E_+}(x)$ thus displays a distinct blueshift of the 0−1 transition frequency. Besides the shift in the 0−1 transition frequency, electronic state mixing also alters the minima of the involved potential curves.

In special cases when the coupling constant β equals zero or the initial geometry difference $\Delta R_{e,A\to B}$ is zero, no change occurs in the curvature of the potential curves $V_{E_+}(x)$ and $V_{E_-}(x)$, nor in the nuclear positions or vibrational states.

In the following, we will illustrate the variation in the 0−1 fundamental Raman transition frequency and the expected equilibrium position $\langle 0|x|0\rangle$ of the new electronic states induced by state mixing.

Variation of the 0−1 Raman Transition Frequency on Lower Electronic State $V_{E_-}(x)$ after Electronic State Mixing

Figure 2 plots the variation of the 0−1 transition frequency induced by electronic state mixing as a function of coupling constants β and adiabatic energy gaps $\Delta E_{e,A\to B}$ with various initial geometry difference values $\Delta R_{e,A\to B}$ ranging from 0.2 to 5.0.

In the nine contour plots in Figure 2, a consistent valley is observed, marking the region of maximum red-shift in the 0−1 transition frequency. The valley deepens and extends toward larger coupling constants as the initial geometry difference, $\Delta R_{e,A\to B}$ increases. For an initial geometry difference $\Delta R_{e,A\to B}$ of 0.2, the minimum of the valley corresponds to a 0−1 transition frequency of approximately 0.97. This minimum value decreases progressively to 0.92, 0.88, 0.80, 0.73, 0.5, 0.3, 0.2, and 0.1 as $\Delta R_{e,A\to B}$ increases from 0.4 to 0.6, 0.8, 1.0, 2.0, 3.0, 4.0, and 5.0, respectively.

When the adiabatic energy gap $\Delta R_{e,A\to B}$ is small, the 0−1 transition frequency initially decreases with an increasing coupling constant β, reaches the valley minimum, and then gradually increases. This indicates that for adiabatic energy gaps less than 2.0, a single redshift may correspond to two distinct coupling constant values. In contrast, when the adiabatic energy gap $\Delta R_{e,A\to B}$ is large (e.g., greater than 3.0), the 0−1 transition frequency decreases monotonically as the coupling constant increases.

Variation of the 0−1 Raman Transition Frequency on Upper Electronic State $V_{E_+}(x)$ after Electronic State Mixing

In the avoided crossing region, the 0−1 transition frequency on potential $V_{E_+}(x)$ exhibits a blue shift relative to the original potentials A and B (each with a 0−1 transition frequency of 1.0) prior to mixing. This blue shift arises from the compressed potential between the inner branches of the original potential curves A and B, as depicted in Figure 1. A larger initial geometry difference $\Delta R_{e,A\to B}$ corresponds to a more pronounced compression of the potential between the inner branches of potentials A and B. Across all nine plots in Figure 3, the maximum blue shift occurs at small energy gaps and weak coupling constants β.

As the initial geometry difference $\Delta R_{e,A\to B}$ increases, the blue-shifted region broadens and its peak value increases. For example, when $\Delta R_{e,A\to B}$ equals 0.2, the maximum blue shift is approximately 1.06; as it increases to 0.4, 0.8, 2.0, and 5.0, the 0−1 transition frequency maxima reach 1.12, 1.22, 1.55, and 2.30, respectively.

When the initial geometry difference $\Delta R_{e,A\to B}$ is small (for instance $\Delta R_{e,A\to B} < 1.0$), there is a peak showing up in the of left-bottom corner of the plots, where both the energy gap $\Delta R_{e,A\to B}$ and coupling constant β is small. For large initial geometry differences $\Delta R_{e,A\to B}$, the 0−1 transition frequency shows reduced sensitivity to the adiabatic energy gap $\Delta R_{e,A\to B}$, becoming predominantly sensitive to the coupling constant β, with the blue shift decreasing as β increases.

Variation of Equilibrium Position $\langle 0|x|0\rangle$ on Lower Electronic State $V_{E_-}(x)$ after Electronic State Mixing

In general, when $\beta \neq 0$ and $\Delta_{Re,A\to B} \neq 0$, the state mixing between A and B modifies the potential curve. In Figure 4, we plot the electronic state mixing introduced variation of the equilibrium position $\langle 0|x|0\rangle$ on the upper electronic state $V_{E_-}(x)$.

https://doi.org/10.1021/acs.jpclett.5c04115
J. Phys. Chem. Lett. XXXX, XXX, XXX−XXX

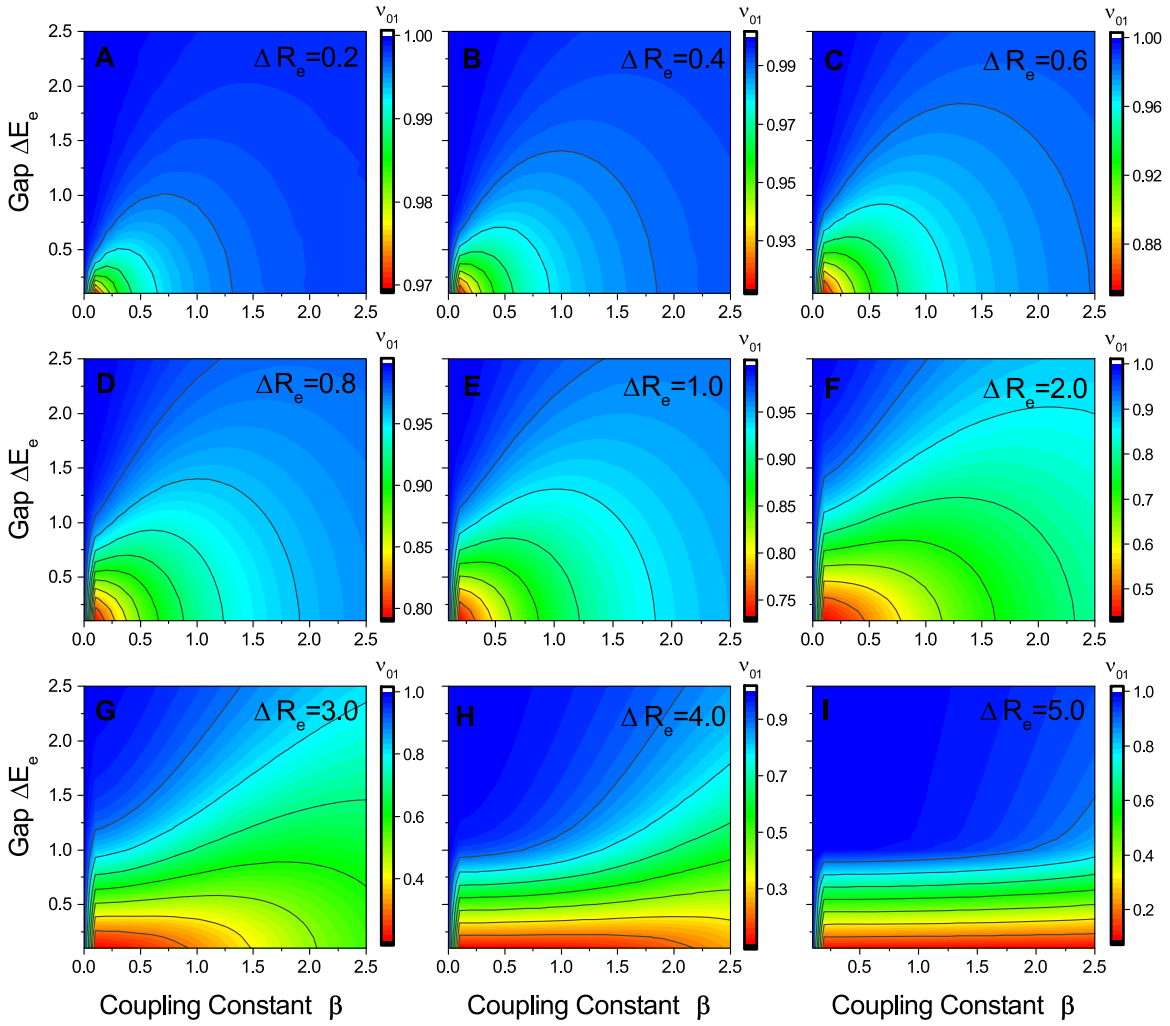

Figure 2. Electronical state mixing introduced variation of the 0−1 transition frequencies of the $V_{E-}(x)$ state as a function of the initial geometry difference ΔR_e: (A) 0.2, (B) 0.4, (C) 0.6, (D) 0.8, (E) 1.0, (F) 2.0, (G) 3.0, (H), 4.0, and (I) 5.0.

When the initial geometry difference between states A and B is small ($\Delta R_{e,A\to B} < 2.0$), the expected position variation is approximately proportional to $\Delta R_{e,A\to B}$. As $\Delta R_{e,A\to B}$ increases, the variation in the mixed position slows, reaches a maximum, and subsequently decreases.

For cases with the same energy gap between states A and B, stronger coupling constants yield greater modification of the molecular geometry and larger expected values of $\langle 0|x|0\rangle$ on $V_{E-}(x)$. In the small energy gap regime, the maximum variation grows with the coupling constant until approaching the midpoint of the equilibrium positions of states A and B, $\frac{R_{e,A}+R_{e,B}}{2}$.

Variation of the Equilibrium Position ⟨0|x|0⟩ on the Upper Electronic State $V_{E+}(x)$ after Electronic State Mixing

Figure 5 presents the variation of the equilibrium position $\langle 0|x|0\rangle$ in the upper electronic state induced by state mixing. Generally, when the initial geometry difference is small ($\Delta R_{e,A\to B} < 1.0$), the $V_{E_+}(x)$ equilibrium geometry $\langle 0|x|0\rangle$ resembles that of potential curve B prior to state mixing within the weak coupling regime. The initial geometry difference determines $\Delta R_{e,A\to B}$ as the amplitude of the largest averaged position $\langle 0|x|0\rangle$ following electronic state mixing. Larger initial geometry differences $\Delta R_{e,A\to B}$ contribute to larger final displacements when the coupling constant β is significantly larger than the energy gap $\left|\frac{\beta}{\Delta E_{e,A\to B}}\right| \to \infty$, i.e., within the strong coupling regime when $\left|\frac{\beta}{\Delta E_{e,A\to B}}\right| \to \infty$, the new equilibrium position shifts to $\frac{X_{e,A}+X_{e,B}}{2}$.

All plots in Figure 5 show a weak coupling strength region, depicted as an upper-left red triangular area, where $\frac{\beta}{\Delta E_{e,A\to B}+\frac{\Delta R_{e,A\to B}^2}{2}} < 0.4$. When the initial geometry difference $\Delta R_{e,A\to B}$ is small, rendering $\frac{\Delta R_{e,A\to B}^2}{2} \ll \Delta E_{e,A\to B}$, the weak coupling region is clearly manifested as an upper-left red triangle in plots A through C in Figure 5. The green regions in plots A−G correspond to medium coupling strength, while the blue regions indicate strong coupling strength. As the initial geometry difference $\Delta R_{e,A\to B}$ increases, the red triangular regions shift and elongate toward regions of larger coupling constants β.

Distinct from the expectation position $\langle 0|x|0\rangle$ on curve $V_{E-}(x)$, the expectation position $\langle 0|x|0\rangle$ on curve $V_{E_+}(x)$ is more sensitive to variations in the adiabatic energy gap $\Delta E_{e,A\to B}$ rather than the coupling constant β.

https://doi.org/10.1021/acs.jpclett.5c04115
J. Phys. Chem. Lett. XXXX, XXX, XXX−XXX

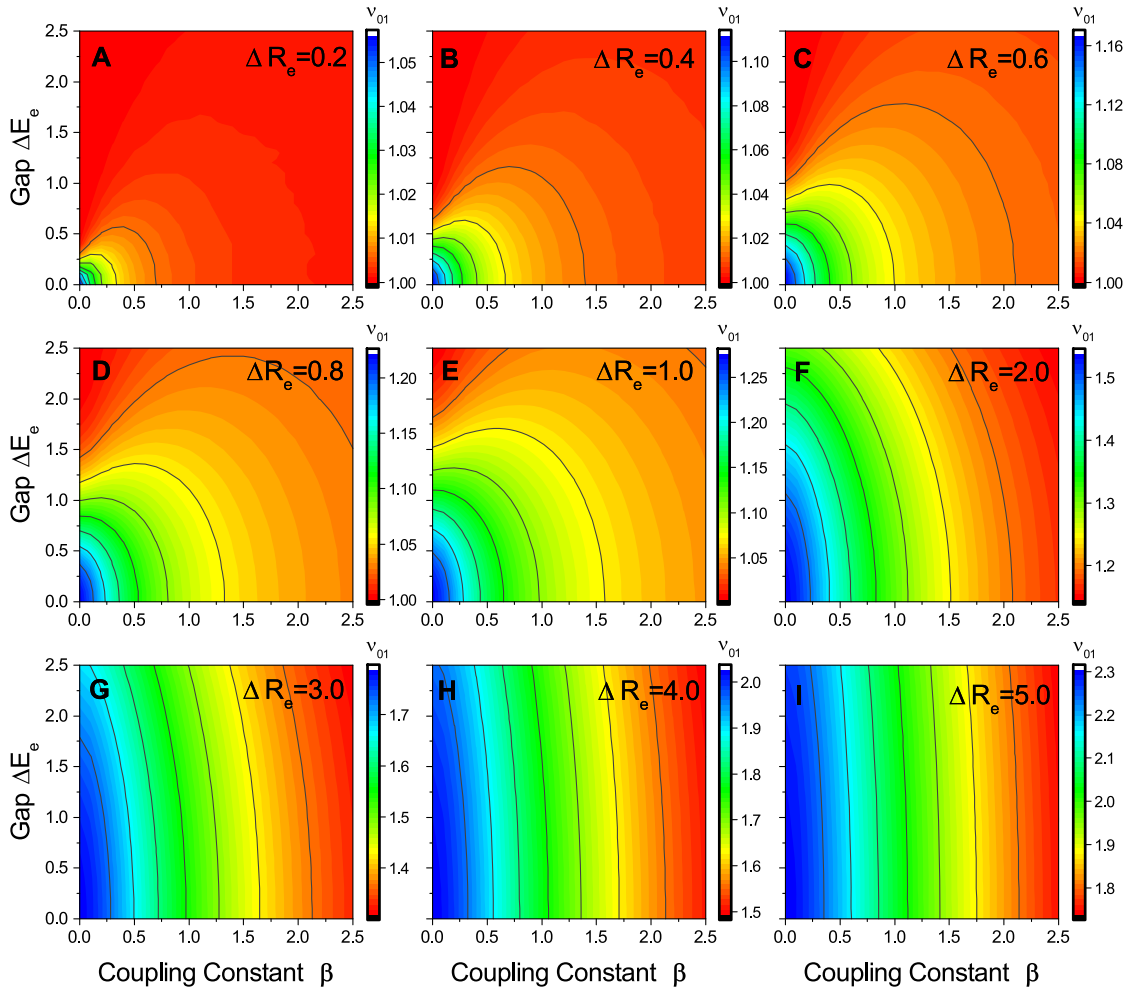

Figure 3. Electronical state mixing introduced variation of the 0−1 transition frequencies of the $V_{E+}(x)$ state as a function of the initial geometry difference ΔR_e: (A) 0.2, (B) 0.4, (C) 0.6, (D) 0.8, (E) 1.0, (F) 2.0, (G) 3.0, (H), 4.0, and (I) 5.0.

Transfer of the 0−1 Transition Frequency Shift from Local Modes to Normal Modes

In the preceding analysis, we investigated the effects of electronic state mixing on isolated local vibrators while neglecting their coupling with other vibrational modes. To address more general scenarios, it is essential to elucidate how frequency shifts originating from local modes are transferred to normal modes. To establish this relationship, we first consider a system comprising two coupled oscillators with unperturbed energies of **0** and **E**, coupled through a coupling constant $\boldsymbol{\beta}$.

$$\hat{\boldsymbol{H}} = \begin{pmatrix} 0 & \beta \\ \beta & E \end{pmatrix} \tag{1}$$

Following diagonalization, the system eigenvalues are transformed accordingly.

$$E_{\pm} = \frac{1}{2}(E \pm \sqrt{E^2 + 4\beta^2}) \tag{2}$$

The corresponding eigenvectors

$$\boldsymbol{\Psi}_{\pm} = \begin{pmatrix} L_{\pm_1} \\ L_{\pm_2} \end{pmatrix}(\varphi_1 \quad \varphi_2) = N^* \begin{pmatrix} \beta \\ \dfrac{E \pm \sqrt{E^2 + 4\beta^2}}{2} \end{pmatrix}(\varphi_1 \quad \varphi_2)$$

are obtained with a normalizing factor $N = \frac{1}{2}[(E \pm \sqrt{E^2 + 4\beta^2})^2 + 4\beta^2]^{1/2}$. Here, the eigenvector matrix elements represent the normalized amplitudes of each component.

$$(L_{\pm_1})^2 = \frac{1}{2}\left(1 \mp \frac{E}{\sqrt{E^2 + 4\beta^2}}\right) \tag{3a}$$

$$(L_{\pm_2})^2 = \frac{1}{2}\left(1 \pm \frac{E}{\sqrt{E^2 + 4\beta^2}}\right) \tag{3b}$$

The derivative of the eigenenergy with respect to E can subsequently be evaluated.

$$\frac{dE_{\pm}}{dE} = \frac{1}{2}\left(1 \pm \frac{E}{\sqrt{E^2 + 4\beta^2}}\right) = (L_{\pm_2})^2 \tag{4}$$

For the generalized case involving N coupled oscillators, the system is described by an $N \times N$ dimensional Hamiltonian matrix $\hat{\boldsymbol{H}}$ with coupling constants $H_{ij} = H_{ji} = \beta_{ij}$ representing the coupling strength between different local modes i and j.

Upon diagonalizing the Hamiltonian matrix, the eigenenergy values of the normal modes and their corresponding eigenvectors are obtained.

https://doi.org/10.1021/acs.jpclett.5c04115
J. Phys. Chem. Lett. XXXX, XXX, XXX−XXX

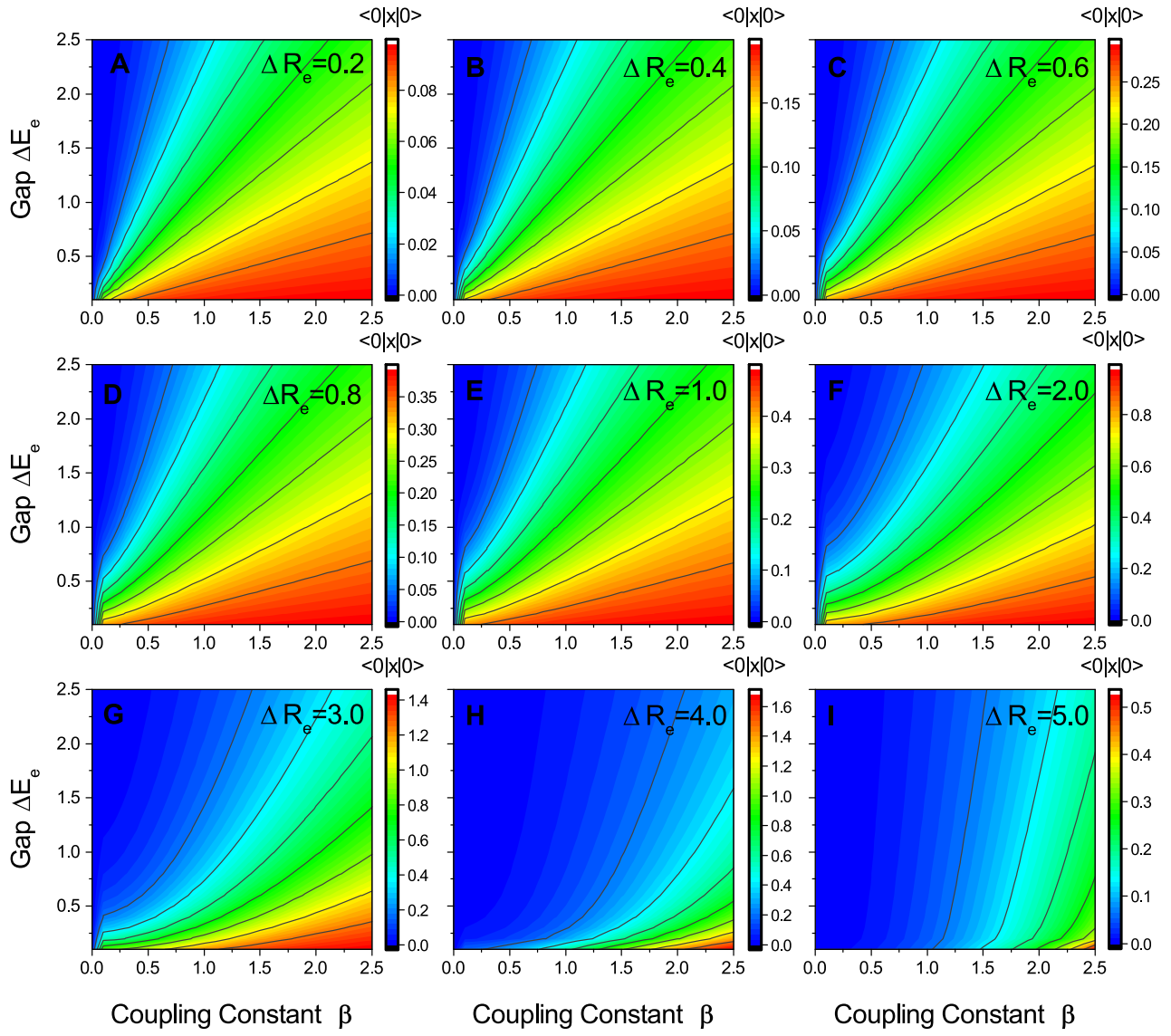

Figure 4. Electronical state mixing introduced variation of the expected position $\langle 0|x|0\rangle$ on $V_{E-}(x)$ as a function of the initial geometry difference ΔR_e: (A) 0.2, (B) 0.4, (C) 0.6, (D) 0.8, (E) 1.0, (F) 2.0, (G) 3.0, (H) 4.0, and (I) 5.0.

$$\hat{H}L = EL \tag{5}$$

Here, E denotes the diagonal eigenenergy matrix of the Hamiltonian matrix $\hat{\boldsymbol{H}}$, with the normalized eigenvectors comprising the columns of the transformation matrix $\boldsymbol{L}$. Here L is an orthogonal matrix, with $\sum_{i=1}^{n}(L_{ij})^2 = 1$, $\sum_{i=1,j\neq k}^{n} L_{ij}L_{ik} = 0$, and $\sum_{i=1,j\neq k}^{n} L_{ji}L_{ki} = 0$.

Reformulating this relationship yields the following expression:

$$L^{-1}\hat{H}L = E \tag{6}$$

Consequently, the eigenenergy of the i^{th} normal mode can be expressed as follows:

$$E_i = E_{ii} = \sum_{j=1}^{n}\sum_{k=1}^{n} L^{-1}{}_{ij}H_{jk}L_{ki} \tag{7}$$

Since the Hamiltonian matrix is symmetric, the transformation matrix satisfies $L^{-1} = L^{\mathrm{T}}$, i.e., $L^{-1}{}_{ij} = L_{ji}$.

$$E_i = \sum_{j=1}^{n}\sum_{k=1}^{n} L_{ji}H_{jk}L_{ki} \tag{8}$$

Separating this equation into two distinct components provides further insight.

$$E_i = \sum_{j=1}^{n}\sum_{k=j}^{n} L_{ji}H_{jk}L_{ki} + \sum_{j=1}^{n}\sum_{k=1,k\neq j}^{n} L_{ji}H_{ki}L_{jk} \tag{9}$$

$$E_i = \sum_{j=1}^{n} (L_{ji})^2 H_{jj} + \sum_{j=1}^{n}\sum_{k=1,k\neq j}^{n} L_{ji}L_{ki}\beta_{jk} \tag{10}$$

Assuming that variations in the coupling constants β_{jk} and the eigenvector elements L_{ki} remain negligible, variation of the normal mode eigenenergy $E_{n,i}$ as a function of changes in the local mode frequency H_{jj} can be approximated as follows:

$$\frac{\partial E_{n,i}}{\partial H_{jj}} = (L_{jn})^2 \tag{11}$$

https://doi.org/10.1021/acs.jpclett.5c04115
J. Phys. Chem. Lett. XXXX, XXX, XXX−XXX

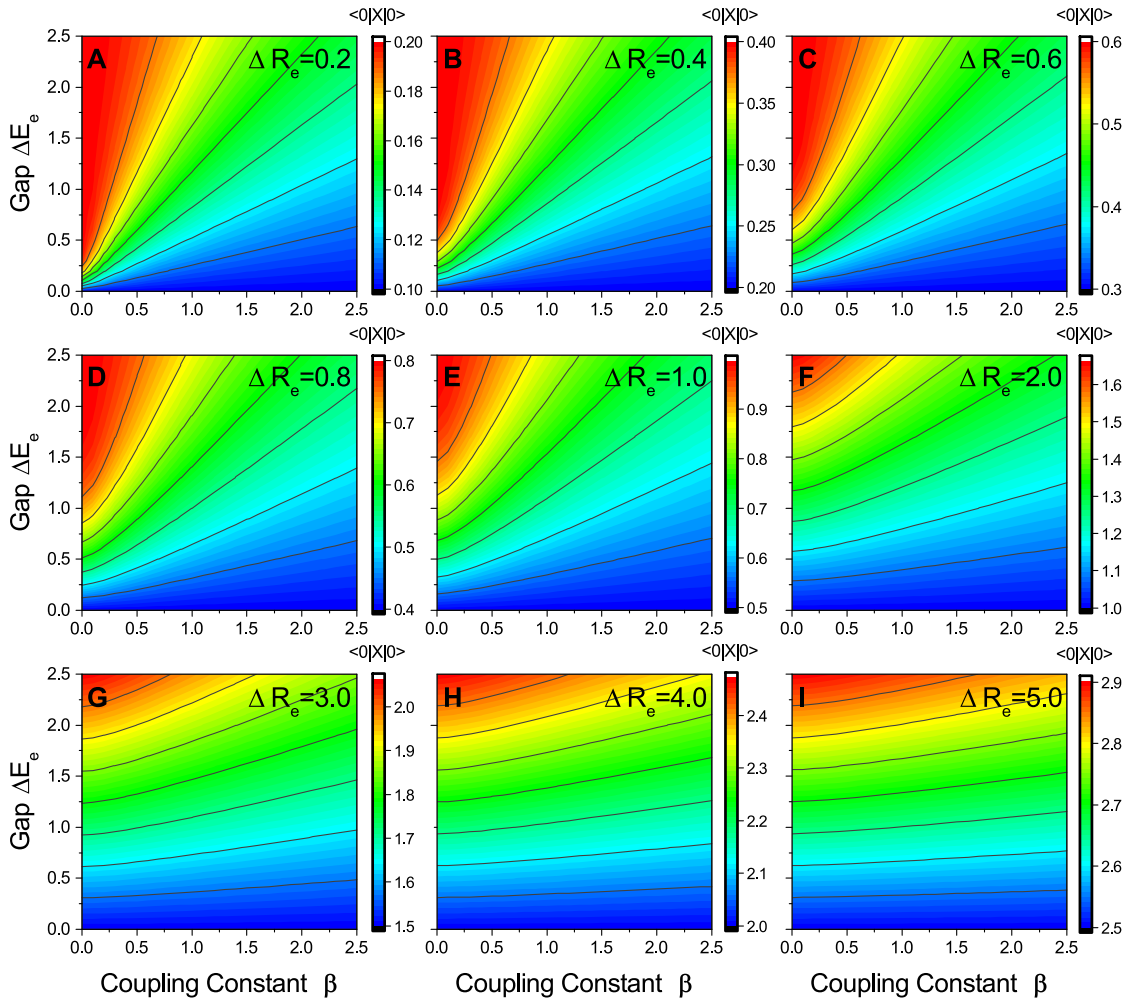

Figure 5. Electronical state mixing introduced variation of the expected position $\langle 0|x|0\rangle$ on $V_{E+}(x)$ as a function of the initial geometry difference ΔR_e: (A) 0.2, (B) 0.4, (C) 0.6, (D) 0.8, (E) 1.0, (F) 2.0, (G) 3.0, (H) 4.0, and (I) 5.0.

This relationship demonstrates that the frequency shift of the normal mode is directly proportional to the squared magnitude of the eigenvector element $(L_{jn})^2$. Consequently, information regarding the element L_{jn} can be extracted from the observed frequency shift of the normal mode.

Frequency Shifts in the Excited-State Raman of Free FMN and the LOV Domain Protein EL222

In our previous work,[30] we compared the calculated geometry differences between the S_1 and S_2 states of MIA as a model for FMN with the corresponding Raman intensity changes.[52] We proposed that there is possible electronic state mixing between the S_1 and S_2 states in EL222. In this study, we further compare the geometry differences between the T_1 and T_2 states, as summarized in Table 1.

The differences in electronic structure and initial geometry $\Delta R_{e,A\rightarrow B}$ across spin states originate from variations in electron−electron coupling between the singlet and triplet states. Pauli repulsion among electrons leads to distinct electron−electron coupling behaviors in states with different spin multiplicities. For MIA, the electronic structures of the S_1 and T_1 states are remarkably similar, both exhibiting a dominant $\pi \rightarrow \pi^*$ transition character.[52,70] This similarity results in comparable chemical bond lengths, as indicated in Table 1. In contrast, the T_2 state exhibits a significantly different electronic structure compared to the S_2 state, with a smaller contribution from n → π^* character (−0.14 in T_2 vs 0.44 in S_2). This electronic discrepancy accounts for the substantial differences in bond lengths presented in Table 1, suggesting distinct bond variation patterns between the S_1−S_2 and T_1−T_2 pairs.

The most pronounced variation in the bond length between S_1 and S_2 occurs for the N_1−C_2 bond (−9 pm) and the C_2═O_2 bond (+9 pm). In FSRS experiments, a total red-shift of approximately 20 cm^{-1} is observed for the Raman-active N_1−C_2 stretching modes in the S_1 state, with frequencies recorded at 1416 (−4) cm^{-1}, 1383 (−9) cm^{-1}, and 1200 (−7) cm^{-1}. This shift corresponds to about 1.5% of the averaged 0−1 Raman transition energy of these three C_1−N_2 stretching modes.

This result implies that electronic state mixing induces a red-shift of roughly 20 cm^{-1} for the C_2═O_2 stretching mode. However, experimental data show a blueshift of 6 cm^{-1}, indicating fewer and weaker hydrogen bonds within the EL222 binding pocket.

In contrast to the bond length variations in singlet states, the largest change between the T_1 and T_2 states occurs in the C_{4a}−N_5 bond (−5 pm). The total redshift of the corresponding Raman-active C_{4a}−N_5 stretching modes in the T_1 state of free FMN is about 5 cm^{-1}, representing approximately 0.35% of the averaged 0−1 transition energy of these modes, which occur at 1515 (−10) cm^{-1}, 1391 (+1) cm^{-1}, and 1269 (+4) cm^{-1} in the T_1 state of free (EL222-bound) FMN. The largest shift observed

https://doi.org/10.1021/acs.jpclett.5c04115
J. Phys. Chem. Lett. XXXX, XXX, XXX−XXX

Table 1. Selected[52,64,70] Chemical Bond Lengths (pm) of Different Electronic States of 10-Methylisoalloxazine (MIA) and Lumiflavin (LF)[a]

		Chemical Bond Length (pm) of Different Electronic States[52,70]							
	LF in S_0	MIA in S_0	MIA S_1	LF in S_1[60]	MIA S_2	Variation MIA S_2-S_1	MIA T_1	MIA T_2	Variation MIA T_2-T_1
$N_1—C_2$	138.0	138.1	140	141	131	−9	138	138	0
$C_2—N_3$	141.4	141.4	138	136	136	−2	138	141	+3
$N_3—C_4$	137.9	137.9	142	140	143	+1	140	138	−2
$C_4—C_{4a}$	150.0	150.2	145	145	145	0	147	146	−1
$C_{4a}—N_5$	129.3	129.0	136	139	136	0	137	132	−5
$N_5—C_{5a}$	136.6	136.9	134	131	134	0	134	135	−1
$C_{5a}—C_6$	140.5	140.5		144					
$C_6—C_7$	138.0	137.8		138					
$C_7—C_8$	142.1	140.1		144					
$C_8—C_9$	138.8	138.4		139					
$C_9—C_{9a}$	140.1	140.3		142					
$C_{9a}—N_{10}$	138.5	138.6		135					
$N_{10}—C_{10a}$	138.2	138.2		137					
$C_{10a}—N_1$	130.1	129.9		136					
$C_{5a}—C_{9a}$	141.5	141.9	145	146	143	−2	145	143	−2
$C_{4a}—C_{10a}$	146.1	146.2	142	137	141	−1	141	144	+3
$C_{10}—R$	146.7	146.8		147					
$C_2—O_2$	121.2	121.1	121.1	119	130	+9	121	121	0
$C_4—O_4$	121.1	121.0		119	121	0	121	121	0

[a]An empty cell indicates a variation less than 1 pm relative to the ground-state S_0 geometry.[52] [Adaption of data presented by Salzmann.[52] Reprinted with permission of Elsevier (copyright 2008).]

Table 2. Vertical Singlet and Triplet Excitation Energies E [eV] of 10-Methylisoalloxazine (MIA) and Lumiflavin (LF)[a,52]

State		Electronic structure (MIA)	MIA	LF
S_0	$1^1A'$	(0.95) Ground state	0	0
S_1	$2^1A'$	$(0.83)\pi_H \rightarrow \pi_L$	3.00	2.94
S_2	$1^1A''$	$(0.44)n_{O2} \rightarrow \pi_L^* - (0.33)n_{N2} \rightarrow \pi_L^*$	3.18	3.21
S_2-S_1			0.23^A	0.27^A
T_1	$1^3A'$	$(0.85)\pi_H \rightarrow \pi_L$	2.30	2.24
T_2	$1^3A''$	$(-0.14)n_{O2} \rightarrow \pi_L^* + (0.59)n_{N2} \rightarrow \pi_L^*$	2.87^A	2.90^A
T_2-T_1			0.52^A	0.66^A
Method			DFT/MRCI(TZVP)	DFT/MRCI(TZVP)

[a]The superscript "A" denotes the adiabatic energy gap between two electronic states. [Adaption of data presented by Salzmann.[52] Reprinted with permission of Elsevier (copyright 2008).].

in the 1505 cm^{-1} mode indicates the dominant contribution of the $C_{4a}-N_5$ bond among these three modes, consistent with the assignment reported by Iuliano and co-workers.[37,71]

Considering the force constants of C═O (1200−1300 N/m) and C═N (900−1000 N/m) double bonds, the initial geometry differences of +9 pm and − 9 pm correspond to dimensionless coordinate variation of approximately 0.5−0.6. A bond length difference of 5 pm for the $C_{4a}-N_5$ bond suggests a change of about 0.2−0.3 in dimensionless coordinate.

The observed redshift of N_1-C_2 mode by 1.5% suggests that the energy gap and coupling constant combination lies within the weak-coupling regime (characterized by small coupling and large energy gap) in the upper-left triangular region of Figure 3C. In this region $\left|\frac{\beta}{\Delta E_e}\right| < 0.4$, the redshift increases with the coupling constant β and decreases with the energy gap $\Delta E_{e,S1\rightarrow S2}$.

The behavior of the 0−1 transition frequency, as illustrated in Figure 3A−C, indicates that a smaller initial geometry difference in the $C_{4a}-N_5$ bond in the triplet state results in a smaller Raman peak redshift compared to the C_1-N_2 stretching modes in the singlet state. This consistent with the observation in Figure 4 of our previous work.[30]

In addition to the smaller bond length difference, two other factors contribute to the reduced frequency shift of the $C_{4a}-N_5$ mode relative to that of the N_1-C_2 modes in the singlet states (Table 2).

(1) A larger adiabatic energy gap between the T_1 and T_2 states (0.52 eV) compared to that between the S_1 and S_2 states (0.23 eV) prior to state mixing.

(2) A possibly weaker coupling constant between the T_1 and T_2 states than between S_1 and S_2, due to symmetry breaking in hydrogen bond interactions with the O4 atom of the flavin ring. This is consistent with the reduced n → π^* contribution in T_2 (−0.14) compared to S_2 (0.44).[52]

Intensity Variation of the Raman Bands in Free FMN and LOV Domain Protein EL222

For the excited-state Raman spectra of free FMN and EL222, we neglect structural variations in the Raman excited states, yielding the expression $\Delta\Delta_k = -L_{kj}\Delta R_j^g$.

When Δ_k and $-L_{kj}\Delta R_j^g$ share the same sign (i.e., $\Delta_k\,(-L_{kj}\Delta R_j^g) > 0$), the Raman intensity of the kth mode increases after state mixing. Conversely, if $\Delta_k\,(-L_{kj}\Delta R_j^g) < 0$, a decrease in the corresponding Raman intensity is expected.

https://doi.org/10.1021/acs.jpclett.5c04115
J. Phys. Chem. Lett. XXXX, XXX, XXX−XXX

In the S_1 state Raman spectroscopy, a clear intensity increase of the N_1-C_2 bands is observed when FMN transitions from an aqueous environment to the EL222 binding pocket. This suggests that for all three normal modes k, the product Δk $(-L_{k,N1-C2}\Delta R^g_{N1-C2})$ is positive. In contrast, for triplet-state Raman, the $C_{4a}-N_5$ mode at 1515 (-10) cm^{-1} exhibits a smaller amplitude change in the opposite direction, shown in Figure 4 of ref 30. This behavior may reflect a negative value of $\Delta k(-L_{k,C4a-N5}\cdot\Delta R^g_{C4a-N5})$ and weaker coupling strength between T_1 and T_2 states, induced by symmetry breaking in hydrogen bond interactions within the EL222 binding pocket.

In this work, by considering electronic mixing between two electronic states with displaced parabolic potentials, we investigated key factors influencing the corresponding stimulated Raman signal: (1) the coupling constant, (2) the energy gap, and (3) the initial geometry difference.

We also derived the relationship between the frequency shift in local modes and that in delocalized normal modes, demonstrating that the local mode shift induces a proportional shift in the normal modes with a distribution proportional to the square of the corresponding eigenvector element.

Using the 0−1 transition frequencies, we estimated the force constants of chemical bonds in the flavin ring, assigning the 9 pm bond length changes in N_1-C_2 and $C_2{=}O_2$ to 0.5−0.6 variations in dimensionless coordinates, and the 5 pm change in the $C_{4a}-N_5$ bond to 0.2−0.3.

Applying these findings to FSRS spectroscopy of free FMN and EL222 in excited states, we find that the coupling between the $^1n\pi^*$ singlet state and the $^1\pi\pi^*$ state lies within the weak coupling regime, resulting in an overall redshift of approximately 20 cm^{-1} (less than 1.5%) in the N_1-C_2 stretching modes.

Due to differences in electron−electron interactions, the triplet states T_1 and T_2 exhibit distinct initial geometry variations, with the largest difference arising from the $C_{4a}-N_5$ bond (5 pm). Experimentally, the normal mode with predominant $C_{4a}-N_5$ stretching exhibits a red-shift of approximately 0.35%. The observed small intensity change, manifested as a narrowing of the line width of the 1515 (-10) cm^{-1} band in EL222, aligns with the weaker coupling strength between triplet states T_1 and T_2 and the smaller initial geometry variation compared to the singlet state S_1 and S_2 case.

METHODS

The Effect of Electronic State Mixing on the Potential Curves and the Vibrational States

Two displaced harmonic oscillators, A and B, possessing identical force constants, are employed to investigate the influence of electronic state mixing on the potential curves: $V_A(x) = \frac{1}{2}(x - x_{e,A}) + V_{e,A}$ and $V_B(x) = \frac{1}{2}(x - x_{e,B}) + V_{e,B}$, with $V_{e,B} > V_{e,A}$ and $\Delta R_{e,A\to B} = x_{e,B}-x_{e,A}$. The adiabatic energy gap between the minima of $V_A(x)$ and $V_B(x)$ is $\Delta E_{e,A\to B} = V_{e,B}-V_{e,A}$. The coupling constant between these two states remains constant along coordinate x.

The behavior of this system can be described by the following Hamiltonian:

$$\hat{\boldsymbol{H}} = \begin{pmatrix} V_A(x) & \beta \\ \beta & V_B(x) \end{pmatrix} \tag{12}$$

The eigenvalues of this Hamiltonian can be expressed as

$$V_{E_\pm}(x) = \frac{1}{2}(V_A(x) + V_B(x) \pm \sqrt{(V_B(x) - V_A(x))^2 + 4\beta^2}) \tag{13}$$

with the corresponding eigenfunctions

$$\begin{aligned}\boldsymbol{\Psi}_\pm &= \begin{pmatrix} L_{\pm_1} \\ L_{\pm_2} \end{pmatrix}(\varphi_A \quad \varphi_B) \\ &= N^*\begin{pmatrix} \beta \\ \dfrac{\Delta E_{A\to B} \pm \sqrt{\Delta E_{A\to B}{}^2 + 4\beta^2}}{2} \end{pmatrix}(\varphi_A \quad \varphi_B)\end{aligned} \tag{14}$$

Here, $\Delta E_{A\to B}(x) = V_B(x)-V_A(x)$, and the normalizing factor is

$$\mathrm{N} = \frac{1}{2}[(\Delta E_{A\to B} \pm \sqrt{\Delta E_{A\to B}{}^2 + 4\beta^2})^2 + 4\beta^2]^{1/2} \tag{15}$$

Subsequently, we numerically solve the Schrödinger equation for the system with the new potential $V_{E_\pm}(x)$. The modified Hamiltonian can be written as

$$\hat{H}(x) = T + V_{E_\pm}(x) = \frac{1}{2}\frac{\partial^2}{\partial x^2} + V_{E_\pm}(x) \tag{16}$$

In the numerical simulations, the finite difference method is applied with MATLAB code provided in the Supporting Information. For simplicity, we set $x_{e,A} = 0$ and $V_{e,A} = 0$.

We obtain the eigenvalues and eigenwave functions of the system under the new potential $V_{E_\pm}(x)$. The fundamental (0−1) Raman transition frequency is calculated from the eigenenergy difference between states $|0\rangle$ and $|1\rangle$, as well as the expected position of the system $\langle n|x|n\rangle$. In this work, we use $\langle 0|x|0\rangle$ as the equilibrium position $x_{e,A}$.

The Effect of Electronic State Mixing on the Stimulated Raman Intensity

The relationship between the stimulated Raman intensity and the molecular structure can be described by the imaginary part of the third-order nonlinear susceptibility[29,30]

$$\begin{aligned}\chi^{(3)}_{\mathrm{SRS}} \propto{}& \frac{\langle g_0|M|e_0\rangle^4}{\omega_{\mathrm{vib}} - (\omega_{\mathrm{pump}} - \omega_{\mathrm{Stokes}}) - i\Gamma_{\mathrm{vib}}} \\ &\times\left(\sum_{\nu n}\frac{\langle 0|n'\rangle\langle n'|1\rangle}{\omega_{g0,e\nu} - \omega_{\mathrm{pump}} - i\Gamma_{e\nu}}\right)^2\end{aligned} \tag{17}$$

where $|n\rangle$ denotes the nth eigenfunction of the Raman-excited state potential.

When the displacement between the Raman ground state and the Raman excited state is small, contributions from higher vibrational states on the Raman excited state can be neglected. Thus, the above equation can be simplified as follows:

$$\begin{aligned}\chi^{(3)}_{\mathrm{SRS}} \propto{}& \frac{\langle g_0|M|e_0\rangle^4}{\omega_{\mathrm{vib}} - (\omega_{\mathrm{pump}} - \omega_{\mathrm{Stokes}}) - i\Gamma_{\mathrm{vib}}} \\ &\times\left(\frac{\langle 0|0'\rangle\langle 0'|1\rangle}{\omega_{g0,e0} - \omega_{\mathrm{pump}} - i\Gamma_{e0}} + \frac{\langle 0|1'\rangle\langle 1'|1\rangle}{\omega_{g0,e1} - \omega_{\mathrm{pump}} - i\Gamma_{e1}}\right)^2\end{aligned} \tag{18}$$

In the displaced harmonic oscillator model, we have a further simplified relation with the displacement[24,25,30,72]

https://doi.org/10.1021/acs.jpclett.5c04115
J. Phys. Chem. Lett. XXXX, XXX, XXX−XXX

$$\chi_{SRS}^{(3)} \propto \frac{\langle g_0|M|e_0\rangle^4}{\omega_{vib} - (\omega_{pump} - \omega_{Stokes}) - i\Gamma_{vib}} \times (\Delta_e)^2 \times \left(\frac{1}{\omega_{g0,e0} - \omega_{pump} - i\Gamma_{e0}} - \frac{1}{\omega_{g0,e1} - \omega_{pump} - i\Gamma_{e1}} \right)^2 \quad (19)$$

The displacement associated with the Raman transition for normal mode k can be expressed as follows.[23,73]

$$\Delta_k = \sum_{j=1}^{3N-6} L_{kj} \Delta R_j^{g \to e} \quad (20)$$

Here, $\Delta R_j^{g \to e}$ denotes the displacement of the internal coordinate between the parabolic potentials of the Raman ground state and the Raman excited state, $\Delta R_j^{g \to e} = R_j^e - R_j^g$.

Following electronic state mixing, the equilibrium position (minimum) of the adiabatic potential curve undergoes a shift; specifically, R_j^g and R_j^e change to $R_j^{g\prime}$ and $R_j^{e\prime}$. This results in a modification of the displacement Δ_k, with the amplitude of $\Delta\Delta_k = L_{kj}[(R_j^{e\prime} - R_j^e) - (R_j^{g\prime} - R_j^g)] = L_{kj}[\Delta R_j^e - \Delta R_j^g]$. The overall contribution to the whole displacement Δ_k is $\Delta\Delta_k$ The sign of $\Delta\Delta_k$ and Δ_k determines whether the Raman intensity for vibrational mode k increases or decrease.

■ ASSOCIATED CONTENT

Supporting Information

The Supporting Information is available free of charge at https://pubs.acs.org/doi/10.1021/acs.jpclett.5c04115.

MATLAB codes used to solve the Schrödinger equation for one-dimensional vibrational motion on the one-dimensional adiabatic potential energy curves (PDF)

Transparent Peer Review report available (PDF)

■ AUTHOR INFORMATION

Corresponding Author

Yingliang Liu − *Institute of Biotechnology of the Czech Academy of Sciences, BIOCEV, CZ-252 50 Vestec, Czechia; ELI Beamlines Facility, The Extreme Light Infrastructure ERIC, 25241 Dolní Břežany, Czech Republic;* orcid.org/0000-0002-4089-688X; Email: liuyl.sino@qq.com

Authors

Alessandra Picchiotti − *Fakultät für Mathematik, Informatik und Naturwissenschaften, Institut für Nanostruktur- und Festkörperphysik, Hamburg Advanced Research Centre for Bioorganic Chemistry (Harbor), DE-22761 Hamburg, Germany; Faculty of Science and Engineering, Groningen Biomolecular Sciences and Biotechnology, Membrane Enzymology Group, University of Groningen, 9747 AG Groningen, Netherlands*

Aditya S. Chaudhari − *Institute of Biotechnology of the Czech Academy of Sciences, BIOCEV, CZ-252 50 Vestec, Czechia*

Mateusz Rebarz − *ELI Beamlines Facility, The Extreme Light Infrastructure ERIC, 25241 Dolní Břežany, Czech Republic*

Miroslav Kloz − *ELI Beamlines Facility, The Extreme Light Infrastructure ERIC, 25241 Dolní Břežany, Czech Republic*

Martin Precek − *ELI Beamlines Facility, The Extreme Light Infrastructure ERIC, 25241 Dolní Břežany, Czech Republic*

Jakob Andreasson − *ELI Beamlines Facility, The Extreme Light Infrastructure ERIC, 25241 Dolní Břežany, Czech Republic*

Gustavo Fuertes − *Institute of Biotechnology of the Czech Academy of Sciences, BIOCEV, CZ-252 50 Vestec, Czechia;* orcid.org/0000-0002-8564-8644

Complete contact information is available at: https://pubs.acs.org/10.1021/acs.jpclett.5c04115

Notes

The authors declare no competing financial interest.

■ ACKNOWLEDGMENTS

The work was supported by the projects ADONIS (CZ.02.1.01/0.0/0.0/16_019/0000789) and *ELIBIO* (CZ.02.1.01/0.0/0.0/15_003/0000447) from the European Regional Development Fund and the Ministry of Education, Youth and Sports (MEYS) of the Czech Republic. The Institute of Biotechnology of the Czech Academy of Sciences acknowledges the institutional grant RVO86652036. The authors acknowledge the use of the ELI Beamlines Facility, Extreme Light Infrastructure ERIC. G.F. acknowledges support from the Czech Science Foundation (GACR) project No. 24-11819S. Funding for the Open Access fees was provided by CZECHELIB (Czech Republic Consortium).

■ REFERENCES

(1) Devaquet, A. Avoided Crossings in Photochemistry. *Pure Appl. Chem.* **1975**, *41* (4), 455−473.

(2) Devaquet, A.; Sevin, A.; Bigot, B. Avoided Crossings in Excited States Potential Energy Surfaces. *J. Am. Chem. Soc.* **1978**, *100* (7), 2009−2011.

(3) Shaik, S.; Zilberg, S.; Haas, Y. A Kekulé-Crossing Model for the "Anomalous" Behavior of the B2u Modes of Aromatic Hydrocarbons in the Lowest Excited 1B2u State. *Acc. Chem. Res.* **1996**, *29* (5), 211−218.

(4) Zilberg, S.; Haas, Y. Frequency Upshift in BO2 and CO2+ upon Electronic Excitation: A Twin-State Model Rationalization. *J. Phys. Chem. A* **2011**, *115* (38), 10650−10654.

(5) Fuß, W.; Haas, Y.; Zilberg, S. Twin States and Conical Intersections in Linear Polyenes. *Chem. Phys.* **2000**, *259* (2−3), 273−295.

(6) Singh, P.; Zhang, J.; Engel, D.; Fingerhut, B. P.; Elsaesser, T. Transient Terahertz Stark Effect: A Dynamic Probe of Electric Interactions in Polar Liquids. *J. Phys. Chem. Lett.* **2023**, *14* (24), 5505−5510.

(7) Kang, B. J.; Rohwer, E. J.; Rohrbach, D.; Zyaee, E.; Akbarimoosavi, M.; Ollmann, Z.; Sorohhov, G.; Borgoo, A.; Cascella, M.; Cannizzo, A.; Decurtins, S.; Stanley, R. J.; Liu, S. X.; Feurer, T. Time-Resolved THz Stark Spectroscopy of Molecules in Solution. *Nat. Commun.* **2024**, *15* (1), 1−7.

(8) Zhang, J.; Singh, P.; Engel, D.; Fingerhut, B. P.; Broser, M.; Hegemann, P.; Elsaesser, T. Ultrafast Terahertz Stark Spectroscopy Reveals the Excited-State Dipole Moments of Retinal in Bacteriorhodopsin. *Proc. Natl. Acad. Sci. U. S. A.* **2024**, *121* (26), 1−7.

(9) Lin, C. Y.; Boxer, S. G. Mechanism of Color and Photoacidity Tuning for the Protonated Green Fluorescent Protein Chromophore. *J. Am. Chem. Soc.* **2020**, *142* (25), 11032−11041.

(10) Lin, C. Y.; Boxer, S. G. Unusual Spectroscopic and Electric Field Sensitivity of Chromophores with Short Hydrogen Bonds: GFP and PYP as Model Systems. *J. Phys. Chem. B* **2020**, *124* (43), 9513−9525.

(11) Lin, C. Y.; Romei, M. G.; Oltrogge, L. M.; Mathews, I. I.; Boxer, S. G. Unified Model for Photophysical and Electro-Optical Properties of Green Fluorescent Proteins. *J. Am. Chem. Soc.* **2019**, *141* (38), 15250−15265.

(12) Agathangelou, D.; Roy, P. P.; del Carmen Marín, M.; Ferré, N.; Olivucci, M.; Buckup, T.; Léonard, J.; Haacke, S. Sub-Picosecond C=C Bond Photo-Isomerization: Evidence for the Role of Excited State Mixing. *C. R. Phys.* **2021**, *22* (S2), 111−138.

(13) Manathunga, M.; Yang, X.; Orozco-Gonzalez, Y.; Olivucci, M. Impact of Electronic State Mixing on the Photoisomerization Time Scale of the Retinal Chromophore. *J. Phys. Chem. Lett.* **2017**, *8* (20), 5222−5227.
(14) Manathunga, M.; Yang, X.; Olivucci, M. Electronic State Mixing Controls the Photoreactivity of a Rhodopsin with All- Trans Chromophore Analogues. *J. Phys. Chem. Lett.* **2018**, *9* (21), 6350−6355.
(15) Dietze, D. R.; Mathies, R. A. Femtosecond Stimulated Raman Spectroscopy. *ChemPhysChem* **2016**, *17* (9), 1224−1251.
(16) McCamant, D. W. Femtosecond Stimulated Raman Spectroscopy. *Encyclopedia of Spectroscopy and Spectrometry* **2017**, *121* (8), 597−602.
(17) Kukura, P.; McCamant, D. W.; Mathies, R. A. Femtosecond Stimulated Raman Spectroscopy. *Annu. Rev. Phys. Chem.* **2007**, *58* (1), 461−488.
(18) Buhrke, D.; Hildebrandt, P. Probing Structure and Reaction Dynamics of Proteins Using Time-Resolved Resonance Raman Spectroscopy. *Chem. Rev.* **2020**, *120* (7), 3577−3630.
(19) Ruhman, S.; Joly, A. G.; Nelson, K. A. Time-Resolved Observations of Coherent Molecular Vibrational Motion and the General Occurrence of Impulsive Stimulated Scattering. *J. Chem. Phys.* **1987**, *86* (11), 6563−6565.
(20) Fragnito, H. L.; Bigot, J. Y.; Becker, P. C.; Shank, C. V. Evolution of the Vibronic Absorption Spectrum in a Molecule Following Impulsive Excitation with a 6 Fs Optical Pulse. *Chem. Phys. Lett.* **1989**, *160* (2), 101−104.
(21) Albrecht, A. C. On the Theory of Raman Intensities. *J. Chem. Phys.* **1961**, *34* (5), 1476−1484.
(22) Myers, A. B.; Mathies, R. A.; Tannor, D. J.; Heller, E. J. Excited State Geometry Changes from Preresonance Raman Intensities: Isoprene and Hexatriene. *J. Chem. Phys.* **1982**, *77* (8), 3857−3866.
(23) Heller, E. J.; Sundberg, R. L.; Tannor, D. Simple Aspects of Raman Scattering. *J. Phys. Chem.* **1982**, *86* (10), 1822−1833.
(24) Inagaki, F.; Tasumi, M.; Miyazawa, T. Excitation Profile of the Resonance Raman Effect of β-Carotene. *J. Mol. Spectrosc.* **1974**, *50* (1−3), 286−303.
(25) Blazej, D. C.; Peticolas, W. L. Ultraviolet Resonant Raman Spectroscopy of Nucleic Acid Components. *Proc. Natl. Acad. Sci. U. S. A.* **1977**, *74* (7), 2639−2643.
(26) Peticolas, W. L.; Blazej, D. C. Estimation of the Distortion of the Geometry of Nucleic-Acid Bases in the Excited Electronic State from the Ultraviolet Resonance Raman Intensity of Certain Normal Modes. *Chem. Phys. Lett.* **1979**, *63* (3), 604−608.
(27) Blazej, D. C.; Peticolas, W. L. Ultraviolet Resonance Raman Excitation Profiles of Pyrimidine Nucleotides. *J. Chem. Phys.* **1980**, *72* (5), 3134−3142.
(28) Takayanagi, M.; Hamaguchi, H. O.; Tasumi, M. Probe-Frequency Dependence of the Resonant Inverse Raman Band Shape. *J. Chem. Phys.* **1988**, *89* (7), 3945−3950.
(29) Wei, L.; Min, W. Electronic Preresonance Stimulated Raman Scattering Microscopy. *J. Phys. Chem. Lett.* **2018**, *9* (15), 4294−4301.
(30) Liu, Y.; Chaudhari, A. S.; Picchiotti, A.; Rebarz, M.; Kloz, M.; Přeček, M.; Andreasson, J.; Schneider, B. Excited-State Mixing in the LOV Domain Proteins: Possible Physics behind the Difference in the Transient Absorption and Transient Stimulated Raman Spectroscopy. *J. Phys. Chem. Lett.* **2025**, *16* (16), 4072−4080.
(31) Batignani, G.; Mai, E.; Fumero, G.; Mukamel, S.; Scopigno, T. Absolute Excited State Molecular Geometries Revealed by Resonance Raman Signals. *Nat. Commun.* **2022**, *13* (1), 7770.
(32) Losi, A. Invited Review Flavin-Based Blue-Light Photosensors: A Photobiophysics Update. *Photochem. Photobiol.* **2007**, *83*, 1283−1300.
(33) Repina, N. A.; Rosenbloom, A.; Mukherjee, A.; Schaffer, D. V.; Kane, R. S. At Light Speed: Advances in Optogenetic Systems for Regulating Cell Signaling and Behavior. *Annu. Rev. Chem. Biomol. Eng.* **2017**, *8*, 13−39.
(34) Christie, J. M. Phototropin Blue-Light Receptors. *Annu. Rev. Plant Biol.* **2007**, *58*, 21.
(35) Losi, A.; Gardner, K. H.; Moglich, A. Blue-Light Receptors for Optogenetics. *Chem. Rev.* **2018**, *118*, 10659.
(36) Green, D.; Roy, P.; Hall, C. R.; Iuliano, J. N.; Jones, G. A.; Lukacs, A.; Tonge, P. J.; Meech, S. R. Excited State Resonance Raman of Flavin Mononucleotide: Comparison of Theory and Experiment. *J. Phys. Chem. A* **2021**, *125* (28), 6171−6179.
(37) Iuliano, J. N.; Hall, C. R.; Green, D.; Jones, G. A.; Lukacs, A.; Illarionov, B.; Bacher, A.; Fischer, M.; French, J. B.; Tonge, P. J.; Meech, S. R. Excited State Vibrations of Isotopically Labeled FMN Free and Bound to a Light−Oxygen−Voltage (LOV) Protein. *J. Phys. Chem. B* **2020**, *124* (33), 7152−7165.
(38) Hall, C. R.; Heisler, I. A.; Jones, G. A.; Frost, J. E.; Gil, A. A.; Tonge, P. J.; Meech, S. R. Femtosecond Stimulated Raman Study of the Photoactive Flavoprotein AppABLUF. *Chem. Phys. Lett.* **2017**, *683*, 365−369.
(39) Andrikopoulos, P. C.; Liu, Y.; Picchiotti, A.; Lenngren, N.; Kloz, M.; Chaudhari, A. S.; Precek, M.; Rebarz, M.; Andreasson, J.; Hajdu, J.; Schneider, B.; Fuertes, G. Femtosecond-to-Nanosecond Dynamics of Flavin Mononucleotide Monitored by Stimulated Raman Spectroscopy and Simulations. *Phys. Chem. Chem. Phys.* **2020**, *22* (12), 6538−6552.
(40) Liu, Y.; Chaudhari, A. S.; Chatterjee, A.; Andrikopoulos, P. C.; Picchiotti, A.; Rebarz, M.; Kloz, M.; Lorenz-Fonfria, V. A.; Schneider, B.; Fuertes, G. Sub-Millisecond Photoinduced Dynamics of Free and EL222-Bound FMN by Stimulated Raman and Visible Absorption Spectroscopies. *Biomolecules* **2023**, *13* (1), 161−172.
(41) Weigel, A.; Dobryakov, A.; Klaumünzer, B.; Sajadi, M.; Saalfrank, P.; Ernsting, N. P. Femtosecond Stimulated Raman Spectroscopy of Flavin after Optical Excitation. *J. Phys. Chem. B* **2011**, *115* (13), 3656−3680.
(42) Weigel, A.; Dobryakov, A. L.; Veiga, M.; Pérez Lustres, J. L. Photoinduced Processes in Riboflavin: Superposition of $\Pi\pi^*-n\pi^*$ States by Vibronic Coupling, Transfer of Vibrational Coherence, and Population Dynamics under Solvent Control. *J. Phys. Chem. A* **2008**, *112* (47), 12054−12065.
(43) Kennis, J. T. M.; Crosson, S.; Gauden, M.; van Stokkum, I. H. M.; Moffat, K.; van Grondelle, R. Primary Reactions of the LOV2 Domain of Phototropin, a Plant Blue-Light Photoreceptor. *Biochemistry* **2003**, *42* (12), 3385−3392.
(44) Van Stokkum, I. H. M.; Gauden, M.; Crosson, S.; Van Grondelle, R.; Moffat, K.; Kennis, J. T. M. The Primary Photophysics of the Avena Sativa Phototropin 1 LOV2 Domain Observed with Time-Resolved Emission Spectroscopy. *Photochem. Photobiol.* **2011**, *87* (3), 534−541.
(45) Gil, A. A.; Laptenok, S. P.; French, J. B.; Iuliano, J. N.; Lukacs, A.; Hall, C. R.; Sazanovich, I. V.; Greetham, G. M.; Bacher, A.; Illarionov, B.; Fischer, M.; Tonge, P. J.; Meech, S. R. Femtosecond to Millisecond Dynamics of Light Induced Allostery in the *Avena Sativa* LOV Domain. *J. Phys. Chem. B* **2017**, *121* (5), 1010−1019.
(46) Iuliano, J. N.; Gil, A. A.; Laptenok, S. P.; Hall, C. R.; Tolentino Collado, J.; Lukacs, A.; Hag Ahmed, S. A.; Abyad, J.; Daryaee, T.; Greetham, G. M.; Sazanovich, I. V.; Illarionov, B.; Bacher, A.; Fischer, M.; Towrie, M.; French, J. B.; Meech, S. R.; Tonge, P. J. Variation in LOV Photoreceptor Activation Dynamics Probed by Time-Resolved Infrared Spectroscopy. *Biochemistry* **2018**, *57* (5), 620−630.
(47) Iuliano, J. N.; Collado, J. T.; Gil, A. A.; Ravindran, P. T.; Lukacs, A.; Shin, S.; Woroniecka, H. A.; Adamczyk, K.; Aramini, J. M.; Edupuganti, U. R.; Hall, C. R.; Greetham, G. M.; Sazanovich, I. V.; Clark, I. P.; Daryaee, T.; Toettcher, J. E.; French, J. B.; Gardner, K. H.; Simmerling, C. L.; Meech, S. R.; Tonge, P. J. Unraveling the Mechanism of a LOV Domain Optogenetic Sensor: A Glutamine Lever Induces Unfolding of the Jα Helix. *ACS Chem. Biol.* **2020**, *15* (10), 2752−2765.
(48) Konold, P. E.; Mathes, T.; Weiβenborn, J.; Groot, M. L.; Hegemann, P.; Kennis, J. T. M. Unfolding of the C-Terminal Jα Helix in the LOV2 Photoreceptor Domain Observed by Time-Resolved Vibrational Spectroscopy. *J. Phys. Chem. Lett.* **2016**, *7* (17), 3472−3476.
(49) Hontani, Y.; Mehlhorn, J.; Domratcheva, T.; Beck, S.; Kloz, M.; Hegemann, P.; Mathes, T.; Kennis, J. T. M. Spectroscopic and Computational Observation of Glutamine Tautomerization in the Blue

https://doi.org/10.1021/acs.jpclett.5c04115
J. Phys. Chem. Lett. XXXX, XXX, XXX−XXX

Light Sensing Using Flavin Domain Photoreaction. *J. Am. Chem. Soc.* **2023**, *145* (2), 1040−1052.
(50) Zhu, J.; Mathes, T.; Hontani, Y.; Alexandre, M. T. A.; Toh, K. C. C.; Hegemann, P.; Kennis, J. T. M. M. Photoadduct Formation from the FMN Singlet Excited State in the LOV2 Domain of Chlamydomonas Reinhardtii Phototropin. *J. Phys. Chem. Lett.* **2016**, *7* (21), 4380−4384.
(51) Alexandre, M. T. A.; Domratcheva, T.; Bonetti, C.; van Wilderen, L. J. G. W.; van Grondelle, R.; Groot, M.-L.; Hellingwerf, K. J.; Kennis, J. T. M. Primary Reactions of the LOV2 Domain of Phototropin Studied with Ultrafast Mid-Infrared Spectroscopy and Quantum Chemistry. *Biophys. J.* **2009**, *97* (1), 227−237.
(52) Salzmann, S.; Tatchen, J.; Marian, C. M. The Photophysics of Flavins: What Makes the Difference between Gas Phase and Aqueous Solution? *J. Photochem. Photobiol. A Chem.* **2008**, *198* (2−3), 221−231.
(53) Wang, J.; Liu, Y. J. Vibrationally Resolved Absorption and Fluorescence Spectra of Flavins: A Theoretical Simulation in the Gas Phase. *Journal of the Chinese Chemical Society* **2023**, *70* (3), 669−679.
(54) Climent, T.; González-Luque, R.; Merchán, M.; Serrano-Andrés, L. Theoretical Insight into the Spectroscopy and Photochemistry of Isoalloxazine, the Flavin Core Ring. *J. Phys. Chem. A* **2006**, *110* (50), 13584−13590.
(55) Vu, V.; Gozem, S. Following Flavin's Vibrational Modes to Probe Anharmonicities and Low-Lying Conical Intersections. *J. Phys. Chem. B* **2025**, *129* (50), 12853−12864.
(56) Andrikopoulos, P. C.; Halimeh, H. Extensive TDDFT Benchmark Study of the Resonance Raman Spectra of Lumiflavin. *J. Comput. Chem.* **2025**, *46* (26), 1−25.
(57) Kabir, M. P.; Ghosh, P.; Gozem, S. Electronic Structure Methods for Simulating Flavin's Spectroscopy and Photophysics: Comparison of Multi-Reference, TD-DFT, and Single-Reference Wave Function Methods. *J. Phys. Chem. B* **2024**, *128* (31), 7545−7557.
(58) Le, D. P. N.; Hastings, G.; Gozem, S. Assigning Flavin's Difference-FTIR Spectral Bands in Solution: Frequency and Intensity Shifts in Flavin's 1-Electron and 2-Electron Reduced States. *Phys. Chem. Chem. Phys.* **2025**, *27* (44), 24024−24039.
(59) Ajagbe, S. O.; Ghosh, P.; Gozem, S. Protein Electrostatics Tune the Singlet−Triplet Energy Gap in Natural and Engineered Phototropin Light-Oxygen-Voltage (LOV) Domains. *J. Am. Chem. Soc.* **2026**, *148*, 7707−7722.
(60) Ghosh, P.; Ajagbe, S. O.; Gozem, S. The Photophysical Path to the Triplet State in Light- Oxygen-Voltage (LOV) Domains. *Chem.—Eur. J.* **2025**, *31*, No. e202500117.
(61) Orozco-Gonzalez, Y.; Kabir, M. P.; Gozem, S. Electrostatic Spectral Tuning Maps for Biological Chromophores. *J. Phys. Chem. B* **2019**, *123* (23), 4813−4824.
(62) Kabir, M. P.; Ouedraogo, D.; Orozco-Gonzalez, Y.; Gadda, G.; Gozem, S. An Alternative Strategy for Spectral Tuning of Flavin-Binding Fluorescent Proteins. *J. Phys. Chem. B* **2023**, *127*, 1301.
(63) Elhajj, S.; D'Ascenzi, J.; Ajagbe, S. O.; Orozco-Gonzalez, Y.; Olivucci, M.; Gozem, S. An Automated QM/MM Average Protein Electrostatic Configuration Approach for Flavoproteins: APEC-F 2.0. *J. Chem. Phys.* **2025**, *163* (11), No. 112501.
(64) Salzmann, S.; Silva-Junior, M. R.; Thiel, W.; Marian, C. M. Influence of the LOV Domain on Low-Lying Excited States of Flavin: A Combined Quantum-Mechanics/Molecular-Mechanics Investigation. *J. Phys. Chem. B* **2009**, *113* (47), 15610−15618.
(65) Chang, X.; Gao, Y.; Fang, W.; Cui, G.; Thiel, W. Quantum Mechanics/Molecular Mechanics Study on the Photoreactions of Dark- and Light-Adapted States of a Blue-Light YtvA LOV Photoreceptor. *Angew. Chem., Int. Ed.* **2017**, *56* (32), 9341−9345.
(66) Nakagawa, S.; Weingart, O.; Marian, C. M. Dual Photochemical Reaction Pathway in Flavin-Based Photoreceptor LOV Domain: A Combined Quantum-Mechanics/Molecular-Mechanics Investigation. *J. Phys. Chem. B* **2017**, *121* (41), 9583−9596.
(67) Andrikopoulos, P. C.; Chaudhari, A. S.; Liu, Y.; Konold, P. E.; Kennis, J. T. M.; Schneider, B.; Fuertes, G. QM Calculations Predict the Energetics and Infrared Spectra of Transient Glutamine Isomers in LOV Photoreceptors. *Phys. Chem. Chem. Phys.* **2021**, *23* (25), 13934−13950.
(68) Nash, A. I.; McNulty, R.; Shillito, M. E.; Swartz, T. E.; Bogomolni, R. A.; Luecke, H.; Gardner, K. H. Erratum: Structural Basis of Photosensitivity in a Bacterial Light-Oxygen-Voltage/ Helix-Turn-Helix (LOV-HTH) DNA-Binding Protein (Proceedings of the National Academy of Sciences of the United States of America (2011) 108, 23 (9449−9454) DOI: 10.1073/Pnas. *Proc. Natl. Acad. Sci. U. S. A.* **2012**, *109* (15), 5904.
(69) Chaudhari, A. S; Favier, A.; Tehrani, Z. A.; Koval, T.; Andersson, I.; Schneider, B.; Dohnalek, J.; Cerny, J.; Brutscher, B.; Fuertes, G. Light-dependent flavin redox and adduct states control the conformation and DNA-binding activity of the transcription factor EL222. *Nucleic Acids Research* **2025**, *53*, gkaf215.
(70) Salzmann, S.; Marian, C. M. The Photophysics of Alloxazine: A Quantum Chemical Investigation in Vacuum and Solution. *Photochemical & Photobiological Sciences* **2009**, *8* (12), 1655−1666.
(71) Green, D.; Roy, P.; Hall, C. R.; Iuliano, J. N.; Jones, G. A.; Lukacs, A.; Tonge, P. J.; Meech, S. R. Excited State Resonance Raman of Flavin Mononucleotide: Comparison of Theory and Experiment. *J. Phys. Chem. A* **2021**, *125* (28), 6171−6179.
(72) Blazej, D. C.; Peticolas, W. L. Ultraviolet Resonance Raman Excitation Profiles of Pyrimidine Nucleotides. *J. Chem. Phys.* **1980**, *72* (5), 3134−3142.
(73) Peticolas, W. L.; Rush, T. Ab Initio Calculations of the Ultraviolet Resonance Raman Spectra of Uracil. *J. Comput. Chem.* **1995**, *16* (10), 1261−1270.

https://doi.org/10.1021/acs.jpclett.5c04115
J. Phys. Chem. Lett. XXXX, XXX, XXX−XXX